

Article

Dynamic Modeling and Analysis of Spacecraft with Multiple Large Flexible Structures

Jin Wei ^{1,2,*}, Wei Liu ², Jia Liu ² and Tao Yu ^{2,*}

¹ State Key Laboratory of Mechanics and Control of Mechanical Structures, Nanjing University of Aeronautics and Astronautics, Nanjing 210016, China

² School of Electromechanical and Automotive Engineering, Yantai University, Yantai 264005, China; 202100356006@s.ytu.edu.cn (W.L.); liujiass@s.ytu.edu.cn (J.L.)

* Correspondence: weijin@ytu.edu.cn (J.W.); yt_126@126.com (T.Y.)

Abstract: An analytical dynamic model is presented for a spacecraft with multiple large flexible structures. Based on the partial differential equations (PDEs) of the motion of the solar panel and deployable arm, the governing equations of the main-body and deployable antenna and the boundary conditions at each end point are used to obtain the frequency and mode shapes of the system. Then, the ordinary differential equations (ODEs) of the system can be obtained from the orthogonality relations and mode shape. The influence of the deployable antenna on the frequencies and mode shapes of the spacecraft is investigated. The frequency veering and mode interchanged phenomenon are observed with the variation of the diameter of the deployable antenna. Using the ODEs, the dynamic responses of the spacecraft are calculated to study the influence of the control torque on the attitude and position of the antenna in the attitude maneuver.

Keywords: flexible structures; flexible spacecraft; global mode shapes; orthogonality relations; analytical dynamic model; dynamical characteristic



Citation: Wei, J.; Liu, W.; Liu, J.; Yu, T. Dynamic Modeling and Analysis of Spacecraft with Multiple Large Flexible Structures. *Actuators* **2023**, *12*, 286. <https://doi.org/10.3390/act12070286>

Academic Editor: André Preumont

Received: 16 June 2023

Revised: 9 July 2023

Accepted: 11 July 2023

Published: 13 July 2023



Copyright: © 2023 by the authors. Licensee MDPI, Basel, Switzerland. This article is an open access article distributed under the terms and conditions of the Creative Commons Attribution (CC BY) license (<https://creativecommons.org/licenses/by/4.0/>).

1. Introduction

With the rapid development of space communication technology, the new generation of satellites is required to be multi-functional and have a long life and high performance. Thus the required spacecraft often need installation of solar wings and deployable antennas.

A large deployable antenna structure is widely used to increase the gain of the space-borne antenna [1]. In 2000, the United States successfully launched the commercial communications satellite Thuraya with a 12.25-m aperture and 55 kg mass [2]. Subsequently, the two Thuraya communication satellites launched in 2003 and 2008 used the same deployable antenna [3]. Thomson [4] found that increasing the antenna size within a certain range does not change its structure and that the unit mass does not increase proportionally but shows a significant downward trend. In the design of the spacecraft attitude control, the main source of radiation force is direct exposure to the sun. Bohling et al. [5] studied the torques produced by the radiation forces on the spacecraft. Solar heating of spacecraft causes antennas far from the sun to bend in the direction of satellite rotation, while antennas near the sun bend in the opposite direction of satellite rotation. Palmerini and Sgubini [6] enhanced the stability of the gravity gradient by adjusting the solar reflector and absorption surface.

For the large-scale space-borne annular truss antenna system, the main components include a two-stage flexible deployable arm, deployable annular truss, wire reflection network, and tension network [4]. For such a complex circular truss antenna structure, the use of finite element software is a practical and effective way to analyze its dynamics [7–14]. Mobre et al. [14] established a finite element model for a deployable antenna structure consisting of two flexible deployable arms and an annular truss; the model obtained the first three natural frequencies and modal shapes of the antenna structure, including pitching,

rolling of the annular trusses, and bending vibration of the deployable arms. Based on the finite element method (FEM), Chodimella et al. [13] found that the thermal strain on the antenna can cause great disturbance to the shape, so it is necessary to add sun-visor and multi-layer insulating material to reduce the thermal disturbance amplitude on the system.

Due to the large and flexible structure of spacecraft, the corresponding system modeling, identification, and control problems have become increasingly complex. Based on experimental methods [15–18], Sabatini et al. [16] used a vibration data acquisition method based on image technology to simulate highly flexible solar panels using aluminum sheets for identifying the vibration modes and characteristic frequencies of spacecraft's flexible structures. Ivanov et al. [17] studied the vibration testing methods of spacecraft with elastic elements such as sensors based on direct inverse Piezoelectricity, sensors and accelerometers based on fiber grating, etc. Wang et al. [18] studied centralized vibration control for measuring flexible dynamic behavior using optical cameras instead of attaching intelligent sensors or actuators nearby to separate the vibration of flexible attachments from disturbances. Angeletti et al. [15], based on the design of spacecraft vibration control structure, carried out numerical simulation through a nonlinear orbit simulator and compared the results with those obtained using a baseline PID controller, finding that robust control has better performance.

Although the FEM and experimental methods can provide an effective approach for the dynamic analysis of complex high-dimensional nonlinear systems, it is necessary to understand and extract the dynamic behavior of the system of the finite element model based on tens of thousands of degrees of freedom. Relatively speaking, analytical methods based on analytical or semi-analytical solutions are helpful to grasp the dynamic characteristics of the system and to explore the global dynamic phenomena of the system.

Using the mode functions to describe the elastic deformation of flexible structures can greatly reduce the degree of freedom of the established system dynamics model, which is very suitable for the design of structural vibration controllers. Spacecraft with a very rigid bus have appendages that demonstrate flexible behavior; in these cases, it is convenient to use the cantilever and other constrained boundary modes to obtain the assumed modes. Therefore, the assumed mode method (AMM) is most widely used in the dynamic modeling of flexible spacecraft for which rigid body platforms are dominant [19–23].

For flexible spacecraft in which the inertia of the rigid body platform does not dominate, the assumed mode can no longer accurately describe the real deformation of the flexible component. In this regard, the dynamic model of large flexible spacecraft established using the global mode is more accurate, because the global mode can truly reflect the elastic vibration of each flexible component in the spacecraft and the motion of the rigid body platform. Based on GMM, Hablani [24] conducted a comprehensive study of the dynamic characteristics and control of flexible spacecraft. Hablani [25] pointed out that, in comparison with the AMM, the dynamic model has its accuracy determined by the inertial ratio of the spacecraft system. Because the global mode contains the modal information of the entire system, selecting a small number of global modes can better describe the motion of the system [26], which makes the global mode very suitable for multiple large flexible structures.

In summary, for large flexible spacecraft, compared with the AMM, the dynamic model established by the global mode has lower degrees of freedom and higher accuracy. However, the global mode is not as direct as the assumed mode, and how to accurately obtain the global mode of the system becomes the key point. Based on the development of the GMM, Wei and Cao applied it to the dynamic modeling and analysis of flexible spacecraft with jointed solar wings [27,28], flexible space manipulators [29], and multi-beam jointed structures [30,31].

Based on the methodology in [28,29,31], a rigid-flexible coupled global modal analysis method for the vibration of the rigid-body platform and flexible appendages (solar wing and deployable antenna) of spacecraft is developed, and the influence of the deployable antenna on the frequencies and mode shapes of the spacecraft is investigated. The frequency

veering and mode interchanged phenomenon is observed with the variation of the diameter of the deployable antenna. The explicit orthogonal relationship between the body and the deployable antenna is described, and the global modal shape and orthogonality are used to derive a set of ODEs governing the motion of the system; the dynamic responses of the spacecraft are calculated to investigate the influence of the control torque on the attitude and position of the antenna in the attitude maneuver.

2. Dynamic Modeling for a Spacecraft with Multiple Large Flexible Structures

2.1. Governing Equations of Motion

Consider the planar motion of a spacecraft that consists of a main-body, two solar arrays, a deployable arm, and deployable antenna, as shown in Figure 1. The solar array and deployable arm are modeled as a Euler–Bernoulli beam. The main-body is assumed to be a rigid body. Because the elastic deformation of the deployable antenna is much smaller than that of the solar wing and the deployable arm, the deployable antenna is simplified as a rigid disk.

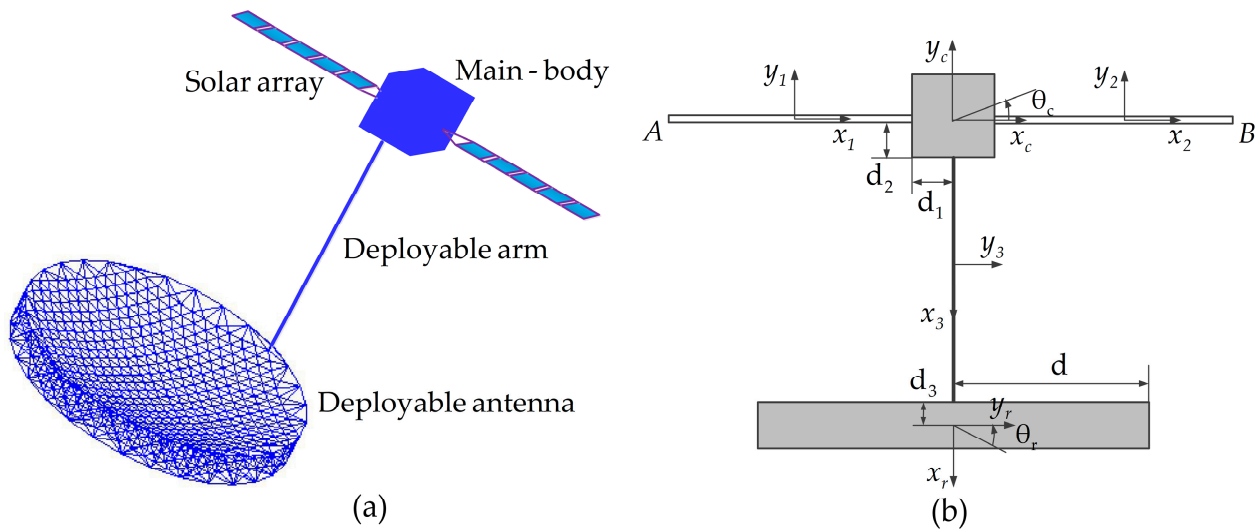


Figure 1. Spacecraft with multiple flexible structures: (a) spatial motion model and (b) planar motion model.

The moment of inertia of the solar array is I_1 , elastic modulus is E_1 , length is L_1 , and mass per unit length is ρ_1 . Similarly, the mass per unit length, elastic modulus, moment of inertia, and length of the deployable arm are denoted by ρ_2 , E_2 , I_2 , and L_2 , respectively. m_c and J_c are the mass and moment of inertia of the main-body, respectively. m_r and J_r are the mass and moment of inertia of the deployable antenna, respectively. d is used to describe the radius of the deployable antenna. Let (x_c, y_c) and (x_r, y_r) be the coordinates of the main-body and deployable antenna, respectively. Let (x_1, y_1) , (x_2, y_2) , and (x_3, y_3) be the coordinates of the left solar array, right solar array, and deployable arm, respectively. θ_c is used to describe the rotational displacement of the main-body, y_c is the translational displacements in the vertical directions, and x_c is the translational displacements in the horizontal direction of the main-body. y_r and θ_r are the translational displacement in the horizontal direction and rotational displacement of the deployable antenna, respectively.

The Euler–Bernoulli beam theory suggests the motion equations of the solar arrays can be expressed as

$$\rho_1 \ddot{v}_i + E_1 I_1 v_i'''' = 0, \quad i = 1, 2. \tag{1}$$

where a prime represents partial differentiation with respect to x , and an overdot represents partial differentiation with regard to time t . v_1 and v_2 are the displacements of the left and right solar arrays, respectively.

Similarly, the motion equation of the deployable arm is expressed as

$$\rho_2 \ddot{v}_3 + E_2 I_2 v_3'''' = 0. \tag{2}$$

where v_3 is the displacement of the deployable arm.

Using the matching conditions, as illustrated in Figure 2a, the motion equations of the main-body for the translation in the horizontal and vertical directions are

$$m_{cx} \ddot{x}_c + E_2 I_2 v_3'''' \left(-\frac{L_2}{2}, t\right) = 0, \tag{3}$$

$$m_{cy} \ddot{y}_c - E_1 I_1 v_1'''' \left(\frac{L_1}{2}, t\right) + E_1 I_1 v_2'''' \left(-\frac{L_1}{2}, t\right) = 0. \tag{4}$$

where $m_{cx} = m_c + 2\rho_1 L_1$ and $m_{cy} = m_c + \rho_2 L_2 + m_r$.

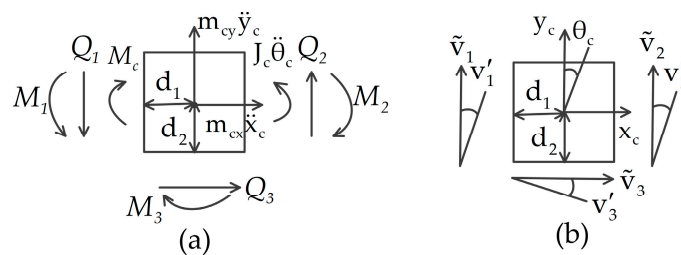


Figure 2. Schematic of the (a) natural and (b) geometrical matching conditions of the main-body: (a) Q_1 , Q_2 , and Q_3 are the shear forces acting on the main-body, $Q_1 = E_1 I_1 v_1'''' \left(L_1/2, t\right)$, $Q_2 = E_1 I_1 v_2'''' \left(-L_1/2, t\right)$, and $Q_3 = E_2 I_2 v_3'''' \left(-L_2/2, t\right)$; M_1 , M_2 , and M_3 are the bending moment acting on the main-body, $M_1 = E_1 I_1 v_1'' \left(L_1/2, t\right)$, $M_2 = E_1 I_1 v_2'' \left(-L_1/2, t\right)$, $M_3 = E_2 I_2 v_3'' \left(-L_2/2, t\right)$; (b) $\tilde{v}_1 = v_1 \left(L_1/2, t\right)$, $v_1' = v_1' \left(L_1/2, t\right)$, $\tilde{v}_2 = v_2 \left(-L_1/2, t\right)$, $v_2' = v_2' \left(-L_1/2, t\right)$, $\tilde{v}_3 = v_3 \left(-L_2/2, t\right)$, and $v_3' = v_3' \left(-L_2/2, t\right)$.

The motion equation of the main-body for the rotation is

$$J_c \ddot{\theta}_c + E_1 I_1 v_1'' \left(\frac{L_1}{2}, t\right) - E_1 I_1 v_2'' \left(-\frac{L_1}{2}, t\right) - E_2 I_2 v_3'' \left(-\frac{L_2}{2}, t\right) + d_1 \left[E_1 I_1 v_1'''' \left(\frac{L_1}{2}, t\right) + E_1 I_1 v_2'''' \left(-\frac{L_1}{2}, t\right)\right] + d_2 E_2 I_2 v_3'''' \left(-\frac{L_2}{2}, t\right) = M_c. \tag{5}$$

where d_1 is the distance from the center of the main-body to the solar array, and d_2 is the distance from the center of the deployable antenna to the deployable arm. The attitude control torque acting on the main-body is denoted by M_c .

As shown in Figure 3a, using the natural matching conditions, the motion equations of the deployable antenna for the translation and rotation are

$$m_r \ddot{y}_r - E_2 I_2 v_3'''' \left(\frac{L_2}{2}, t\right) = 0, \tag{6}$$

$$J_r \ddot{\theta}_r + E_2 I_2 v_3'' \left(\frac{L_2}{2}, t\right) - d_3 E_2 I_2 v_3'''' \left(\frac{L_2}{2}, t\right) = 0. \tag{7}$$

Next, the boundary condition of the spacecraft is analyzed. The geometric matching conditions of the main-body are illustrated in Figure 2b.

$$\begin{cases} v_1 \left(\frac{L_1}{2}, t\right) = y_c - d_1 \theta_c, v_2 \left(-\frac{L_1}{2}, t\right) = y_c + d_1 \theta_c, v_3 \left(-\frac{L_2}{2}, t\right) = x_c + d_2 \theta_c, \\ v_1' \left(\frac{L_1}{2}, t\right) = \theta_c, v_2' \left(-\frac{L_1}{2}, t\right) = \theta_c, v_3' \left(-\frac{L_2}{2}, t\right) = \theta_c. \end{cases} \tag{8}$$

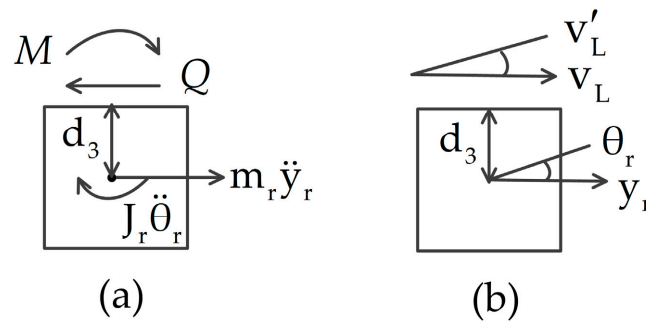


Figure 3. Schematic of the (a) natural and (b) geometrical matching conditions of deployable antenna: (a) Q is the shear force acting on deployable antenna, $Q = E_2 I_2 v_3'''(L_2/2, t)$; M is the bending moment acting on deployable antenna, $M = E_2 I_2 v_3''(L_2/2, t)$; (b) $\tilde{v}_L = v_3(L_2/2, t)$, $v'_L = v_3'(L_2/2, t)$.

The geometric matching conditions of the deployable antenna are depicted in Figure 3b.

$$y_r = v_3\left(\frac{L_2}{2}, t\right) - d_3 \theta_r, \theta_r = v_3'\left(\frac{L_2}{2}, t\right). \tag{9}$$

The A and B of the solar arrays are the free ends of the cantilever beam, with zero bending moment and shear force.

$$\begin{cases} E_1 I_1 v_1''(-\frac{L_1}{2}, t) = 0, E_1 I_1 v_1'''(-\frac{L_1}{2}, t) = 0, \\ E_1 I_1 v_2''(\frac{L_1}{2}, t) = 0, E_1 I_1 v_2'''(\frac{L_1}{2}, t) = 0. \end{cases} \tag{10}$$

2.2. Natural Frequencies and Global Mode Shapes

In order to obtain a low-dimensional dynamic model, it is necessary to study the eigenvalue problem of the system to obtain the global mode shapes. It is assumed that the displacements of the spacecraft are separable in space and time. Where ω is an unknown constant relating to the system's natural frequency, let

$$\begin{aligned} v_i(x, t) &= \varphi_i(x) e^{j\omega t}, & x_c &= X_c e^{j\omega t}, & y_c &= Y_c e^{j\omega t}, & \theta_c &= \Theta_c e^{j\omega t}, \\ x_r &= X_r e^{j\omega t}, & y_r &= Y_r e^{j\omega t}, & \theta_r &= \Theta_r e^{j\omega t}, & i &= 1, 2, 3. \end{aligned} \tag{11}$$

Integrating Equation (11) into Equations (1)–(7) without external force yields

$$\omega^2 \rho_1 \varphi_i(x) - E_1 I_1 \varphi_i''''(x) = 0, \quad i = 1, 2, \tag{12}$$

$$\omega^2 \rho_2 \varphi_3(x) - E_2 I_2 \varphi_3''''(x) = 0, \tag{13}$$

$$\omega^2 m_{cx} X_c - E_2 I_2 \varphi_3'''(-\frac{L_2}{2}) = 0, \tag{14}$$

$$\omega^2 m_{cy} Y_c + E_1 I_1 \varphi_1'''(\frac{L_1}{2}) - E_1 I_1 \varphi_2'''(-\frac{L_1}{2}) = 0, \tag{15}$$

$$\omega^2 J_c \Theta_c - E_1 I_1 \varphi_1''(\frac{L_1}{2}) + E_1 I_1 \varphi_2''(-\frac{L_1}{2}) + E_2 I_2 \varphi_3''(-\frac{L_2}{2}) - d_1 [E_1 I_1 \varphi_1'''(\frac{L_1}{2}) + E_1 I_1 \varphi_2'''(-\frac{L_1}{2})] - d_2 E_2 I_2 \varphi_3'''(-\frac{L_2}{2}) = 0, \tag{16}$$

$$\omega^2 m_r Y_r + E_2 I_2 \varphi_3'''(\frac{L_2}{2}) = 0, \tag{17}$$

$$\omega^2 J_r \Theta_r - E_2 I_2 \varphi_3''(\frac{L_2}{2}) + d_3 E_2 I_2 \varphi_3'''(\frac{L_2}{2}) = 0. \tag{18}$$

The main-body geometric matching conditions are simplified to

$$\begin{cases} \varphi_1(\frac{L_1}{2}) = Y_c - d_1\Theta_c, \varphi_2(-\frac{L_1}{2}) = Y_c + d_1\Theta_c, \varphi_3(-\frac{L_2}{2}) = X_c + d_2\Theta_c, \\ \varphi'_1(\frac{L_1}{2}) = \Theta_c, \varphi'_2(-\frac{L_1}{2}) = \Theta_c, \varphi'_3(-\frac{L_2}{2}) = \Theta_c. \end{cases} \tag{19}$$

The geometric matching conditions of the deployable antenna are reduced to

$$Y_r = \varphi_3(\frac{L_2}{2}) - d_3\Theta_r, \Theta_r = \varphi'_3(\frac{L_2}{2}). \tag{20}$$

The boundary conditions at A and B become

$$\begin{cases} E_1I_1\varphi''_1(-\frac{L_1}{2}) = 0, E_1I_1\varphi'''_1(-\frac{L_1}{2}) = 0, \\ E_1I_1\varphi''_2(\frac{L_1}{2}) = 0, E_1I_1\varphi'''_2(\frac{L_1}{2}) = 0. \end{cases} \tag{21}$$

The solutions of Equations (12) and (13) are

$$\begin{cases} \varphi_1(x) = A_1 \cos(\beta_1x) + B_1 \sin(\beta_1x) + C_1 \cosh(\beta_1x) + D_1 \sinh(\beta_1x), & x \in [0, L_1], \\ \varphi_2(x) = A_2 \cos(\beta_1x) + B_2 \sin(\beta_1x) + C_2 \cosh(\beta_1x) + D_2 \sinh(\beta_1x), & x \in [0, L_1], \\ \varphi_3(x) = A_3 \cos(\beta_2x) + B_3 \sin(\beta_2x) + C_3 \cosh(\beta_2x) + D_3 \sinh(\beta_2x), & x \in [0, L_2]. \end{cases} \tag{22}$$

where $\beta_1 = (\frac{\rho_1\omega^2}{E_1I_1})^{1/4}$ and $\beta_2 = (\frac{\rho_2\omega^2}{E_2I_2})^{1/4}$. Let

$$\psi_i = [A_i \quad B_i \quad C_i \quad D_i], \quad i = 1, 2, 3, \tag{23}$$

$$\psi = [\psi_1 \quad \psi_2 \quad \psi_3 \quad X_c \quad Y_c \quad \Theta_c \quad Y_r \quad \Theta_r]^T. \tag{24}$$

Substituting Equation (22) into Equations (19)–(21), and then determining the main-body and deployable antenna using Equations (14)–(18), the following characteristic equation can be obtained:

$$H(\omega)\psi = 0, \tag{25}$$

where the matrix $H(\omega) \in \mathbb{R}^{17 \times 17}$.

Let $\det(H(\omega)) = 0$. ω_s is the s -th natural frequency, and $\psi^{(s)}$ is the s -th global mode shapes for the system.

2.3. Orthogonality

$\phi_m(x)$ and $\phi_s(x)$ represent the global mode shapes associated with the two unique eigenvalues ω_m and ω_s .

$$\phi_r(x) = [\varphi_1 \quad \varphi_2 \quad \varphi_3 \quad X_{cm} \quad Y_{cm} \quad \Theta_{cm} \quad Y_{rm} \quad \Theta_{rm}]^T, m = 1, 2, \dots. \tag{26}$$

By Equations (12)–(18), one has

$$\omega_m^2 \rho_1 \varphi_{im}(x) = E_1 I_1 \varphi_{im}''''(x), \quad i = 1, 2, \tag{27}$$

$$\omega_m^2 \rho_2 \varphi_{3m}(x) = E_2 I_2 \varphi_{3m}''''(x), \tag{28}$$

$$\omega_m^2 m_{cx} X_{cm} = E_2 I_2 \varphi_{3m}'''(-\frac{L_2}{2}), \tag{29}$$

$$\omega_m^2 m_{cy} Y_{cm} = -E_1 I_1 \varphi_{1m}'''(\frac{L_1}{2}) + E_1 I_1 \varphi_{2m}'''(-\frac{L_1}{2}), \tag{30}$$

$$\omega_m^2 J_c \Theta_{cm} = E_1 I_1 \varphi''_{1m} \left(\frac{L_1}{2}\right) - E_1 I_1 \varphi''_{2m} \left(-\frac{L_1}{2}\right) - E_2 I_2 \varphi''_{3m} \left(-\frac{L_2}{2}\right) + d_1 \left[E_1 I_1 \varphi'''_{1m} \left(\frac{L_1}{2}\right) + E_1 I_1 \varphi'''_{2m} \left(-\frac{L_1}{2}\right) \right] + d_2 E_2 I_2 \varphi'''_{3m} \left(-\frac{L_2}{2}\right), \tag{31}$$

$$\omega_m^2 m_r Y_{rm} = -E_2 I_2 \varphi'''_{3m} \left(\frac{L_2}{2}\right), \tag{32}$$

$$\omega_m^2 J_r \Theta_{rm} = E_2 I_2 \varphi''_{3m} \left(\frac{L_2}{2}\right) - d_3 E_2 I_2 \varphi'''_{3m} \left(\frac{L_2}{2}\right). \tag{33}$$

Then, multiply Equation (27) by φ_{1s} and φ_{2s} ; for the two solar arrays, integrate the resulting equations across the domain $0 \leq x \leq L_1$, respectively; multiply Equation (28) by φ_{3s} ; integrate the resulting equations over the domain $0 \leq x \leq L_2$ for the deployable arm; and add the resulting equations to obtain

$$\int_0^{L_1} E_1 I_1 \varphi''_{1m} (x) \varphi_{1s}(x) dx + \int_0^{L_1} E_1 I_1 \varphi''_{2m} (x) \varphi_{2s}(x) dx + \int_0^{L_2} E_2 I_2 \varphi''_{3m} (x) \varphi_{3s}(x) dx = \omega_m^2 \left(\int_0^{L_1} \rho_1 \varphi_{1m}(x) \varphi_{1s}(x) dx + \int_0^{L_1} \rho_1 \varphi_{2m}(x) \varphi_{2s}(x) dx + \int_0^{L_2} \rho_2 \varphi_{3m}(x) \varphi_{3s}(x) dx \right). \tag{34}$$

Multiply Equations (29)–(33) by X_{cs} , Y_{cs} , Θ_{cs} , Y_{rs} , and Θ_{rs} , respectively, and then sum the resulting equations to obtain

$$\begin{aligned} & E_2 I_2 \varphi'''_{3m} \left(-\frac{L_2}{2}\right) X_{cs} + \left[-E_1 I_1 \varphi'''_{1m} \left(\frac{L_1}{2}\right) + E_1 I_1 \varphi'''_{2m} \left(-\frac{L_1}{2}\right) \right] Y_{cs} \\ & + \left[E_1 I_1 \varphi''_{1m} \left(\frac{L_1}{2}\right) - E_1 I_1 \varphi''_{2m} \left(-\frac{L_1}{2}\right) - E_2 I_2 \varphi''_{3m} \left(-\frac{L_2}{2}\right) \right] \Theta_{cs} \\ & + \left[d_1 E_1 I_1 \varphi'''_{1m} \left(\frac{L_1}{2}\right) + d_1 E_1 I_1 \varphi'''_{2m} \left(-\frac{L_1}{2}\right) + d_2 E_2 I_2 \varphi'''_{3m} \left(-\frac{L_2}{2}\right) \right] \Theta_{cs} \\ & - E_2 I_2 \varphi'''_{3m} \left(\frac{L_2}{2}\right) Y_{rs} + \left[E_2 I_2 \varphi''_{3m} \left(\frac{L_2}{2}\right) + d_3 E_2 I_2 \varphi'''_{3m} \left(\frac{L_2}{2}\right) \right] \Theta_{rs} \\ & = \omega_m^2 [m_{cx} X_{cm} X_{cs} + m_{cy} Y_{cm} Y_{cs} + J_c \Theta_{cm} \Theta_{cs} + m_r Y_{rm} Y_{rs} + J_r \Theta_{rm} \Theta_{rs}]. \end{aligned} \tag{35}$$

Using the boundary and matching conditions in Equations (19)–(21), adding Equation (35), and integrating Equation (34) by parts yields

$$\begin{aligned} & \int_0^{L_1} E_1 I_1 \varphi''_{1m} (x) \varphi_{1s}(x) dx + \int_0^{L_1} E_1 I_1 \varphi''_{2m} (x) \varphi_{2s}(x) dx + \int_0^{L_2} E_2 I_2 \varphi''_{3m} (x) \varphi_{3s}(x) dx = \\ & \int_0^{L_1} E_1 I_1 \varphi''_{1m} (x) \varphi''_{1s}(x) dx + \int_0^{L_1} E_1 I_1 \varphi''_{2m} (x) \varphi''_{2s}(x) dx + \int_0^{L_2} E_2 I_2 \varphi''_{3m} (x) \varphi''_{3s}(x) dx \\ & - \omega_m^2 [m_{cx} X_{cm} X_{cs} + m_{cy} Y_{cm} Y_{cs} + J_c \Theta_{cm} \Theta_{cs} + m_r Y_{rm} Y_{rs} + J_r \Theta_{rm} \Theta_{rs}]. \end{aligned} \tag{36}$$

Substituting Equation (36) into the left-hand side of Equation (34) yields

$$\begin{aligned} & \int_0^{L_1} E_1 I_1 \varphi''_{1m} (x) \varphi''_{1s}(x) dx + \int_0^{L_1} E_1 I_1 \varphi''_{2m} (x) \varphi''_{2s}(x) dx + \int_0^{L_2} E_2 I_2 \varphi''_{3m} (x) \varphi''_{3s}(x) dx \\ & = \omega_m^2 \left[\int_0^{L_1} \rho_1 \varphi_{1m}(x) \varphi_{1s}(x) dx + \int_0^{L_1} \rho_1 \varphi_{2m}(x) \varphi_{2s}(x) dx + \int_0^{L_2} \rho_2 \varphi_{3m}(x) \varphi_{3s}(x) dx \right. \\ & \quad \left. + m_{cx} X_{cm} X_{cs} + m_{cy} Y_{cm} Y_{cs} + J_c \Theta_{cm} \Theta_{cs} + m_r Y_{rm} Y_{rs} + J_r \Theta_{rm} \Theta_{rs} \right]. \end{aligned} \tag{37}$$

Exchanging the superscripts m and s in Equation (37) yields

$$\begin{aligned} & \int_0^{L_1} E_1 I_1 \varphi''_{1m} (x) \varphi''_{1s}(x) dx + \int_0^{L_1} E_1 I_1 \varphi''_{2m} (x) \varphi''_{2s}(x) dx + \int_0^{L_2} E_2 I_2 \varphi''_{3m} (x) \varphi''_{3s}(x) dx \\ & = \omega_s^2 \left[\int_0^{L_1} \rho_1 \varphi_{1m}(x) \varphi_{1s}(x) dx + \int_0^{L_1} \rho_1 \varphi_{2m}(x) \varphi_{2s}(x) dx + \int_0^{L_2} \rho_2 \varphi_{3m}(x) \varphi_{3s}(x) dx \right. \\ & \quad \left. + m_{cx} X_{cm} X_{cs} + m_{cy} Y_{cm} Y_{cs} + J_c \Theta_{cm} \Theta_{cs} + m_r Y_{rm} Y_{rs} + J_r \Theta_{rm} \Theta_{rs} \right]. \end{aligned} \tag{38}$$

Subtracting Equation (37) from Equation (38) yields

$$\begin{aligned} & (\omega_m^2 - \omega_s^2) \left[\int_0^{L_1} \rho_1 \varphi_{1m}(x) \varphi_{1s}(x) dx + \int_0^{L_1} \rho_1 \varphi_{2m}(x) \varphi_{2s}(x) dx + \int_0^{L_2} \rho_2 \varphi_{3m}(x) \varphi_{3s}(x) dx \right] \\ & + (\omega_m^2 - \omega_s^2) [m_{cx} X_{cm} X_{cs} + m_{cy} Y_{cm} Y_{cs} + J_c \Theta_{cm} \Theta_{cs} + m_r Y_{rm} Y_{rs} + J_r \Theta_{rm} \Theta_{rs}] = 0. \end{aligned} \tag{39}$$

The first orthogonality relation can be derived from Equation (39).

$$\int_0^{L_1} \rho_1 \varphi_{1m}(x) \varphi_{1s}(x) dx + \int_0^{L_1} \rho_1 \varphi_{2m}(x) \varphi_{2s}(x) dx + \int_0^{L_2} \rho_2 \varphi_{3m}(x) \varphi_{3s}(x) dx + m_{cx} X_{cm} X_{cs} + m_{cy} Y_{cm} Y_{cs} + J_c \Theta_{cm} \Theta_{cs} + m_r Y_{rm} Y_{rs} + J_r \Theta_{rm} \Theta_{rs} = M_s \delta_{ms}. \tag{40}$$

where M_s is s-th modal mass and δ_{ms} is the Kronecker delta. The second orthogonality relation can be calculated using Equations (37) and (40).

$$\int_0^{L_1} E_1 I_1 \varphi_{1m}''(x) \varphi_{1s}''(x) dx + \int_0^{L_1} E_1 I_1 \varphi_{2m}''(x) \varphi_{2s}''(x) dx + \int_0^{L_2} E_2 I_2 \varphi_{3m}''(x) \varphi_{3s}''(x) dx = K_m \delta_{ms}. \tag{41}$$

where K_s is s – th modal stiffness.

2.4. Dynamic Model with Multi-DOF

By using the global mode shapes obtained by characteristic Equation (25), the displacements of the flexible spacecraft can be written as

$$v_1(x, t) = \sum_{sr=1}^n \varphi_{1sr}(x) q_{sr}(t), \quad v_2(x, t) = \sum_{sr=1}^n \varphi_{2sr}(x) q_{sr}(t), \quad v_3(x, t) = \sum_{sr=1}^n \varphi_{3sr}(x) q_{sr}(t), \tag{42}$$

$$x_c = \sum_{sr=1}^n X_{csr} q_{sr}(t), y_c = \sum_{sr=1}^n Y_{csr} q_{sr}(t), \theta_c = \sum_{sr=1}^n \Theta_{csr} q_{sr}(t), y_r = \sum_{sr=1}^n Y_{rsr} q_{sr}(t), \theta_r = \sum_{sr=1}^n \Theta_{rsr} q_{sr}(t).$$

The sr-th modal coordinate of the system is $q_{sr}(t)$.

Substituting Equation (42) into Equations (1)–(7) yields

$$\rho_1 \sum_{sr=1}^n \varphi_{isr}(x) \ddot{q}_{sr}(t) + E_1 I_1 \sum_{sr=1}^n \varphi_{isr}''''(x) q_{sr}(t) = 0, \quad i = 1, 2, \tag{43}$$

$$\rho_2 \sum_{sr=1}^n \varphi_{3sr}(x) \ddot{q}_{sr}(t) + E_2 I_2 \sum_{sr=1}^n \varphi_{3sr}''''(x) q_{sr}(t) = 0, \tag{44}$$

$$m_{cx} \sum_{sr=1}^n X_{csr} \ddot{q}_{sr}(t) + E_2 I_2 \sum_{sr=1}^n \varphi_{3sr}''''(-\frac{L_2}{2}) q_{sr}(t) = 0, \tag{45}$$

$$m_{cy} \sum_{sr=1}^n Y_{csr} \ddot{q}_{sr}(t) - E_1 I_1 \sum_{sr=1}^n \varphi_{1sr}''''(\frac{L_1}{2}) q_{sr}(t) + E_1 I_1 \sum_{sr=1}^n \varphi_{2sr}''''(-\frac{L_1}{2}) q_{sr}(t) = 0, \tag{46}$$

$$J_c \sum_{sr=1}^n \Theta_{csr} \ddot{q}_{sr}(t) + E_1 I_1 \sum_{sr=1}^n \varphi_{1sr}''(\frac{L_1}{2}) q_{sr}(t) - E_1 I_1 \sum_{sr=1}^n \varphi_{2sr}''(-\frac{L_1}{2}) q_{sr}(t) - E_2 I_2 \sum_{sr=1}^n \varphi_{3sr}''(-\frac{L_2}{2}) q_{sr}(t) + d_1 \left[E_1 I_1 \sum_{sr=1}^n \varphi_{1sr}''''(\frac{L_1}{2}) q_{sr}(t) + E_1 I_1 \sum_{sr=1}^n \varphi_{2sr}''''(-\frac{L_1}{2}) q_{sr}(t) \right] + d_2 E_2 I_2 \sum_{sr=1}^n \varphi_{3sr}''''(-\frac{L_2}{2}) q_{sr}(t) = M_c, \tag{47}$$

$$m_r \sum_{sr=1}^n Y_{rsr} \ddot{q}_{sr}(t) - E_2 I_2 \sum_{sr=1}^n \varphi_{3sr}''''(\frac{L_2}{2}) q_{sr}(t) = 0. \tag{48}$$

$$J_r \sum_{sr=1}^n \Theta_{rsr} \ddot{q}_{sr}(t) + E_2 I_2 \sum_{sr=1}^n \varphi_{3sr}''(\frac{L_2}{2}) q_{sr}(t) - d_3 E_2 I_2 \sum_{sr=1}^n \varphi_{3sr}''''(\frac{L_2}{2}) q_{sr}(t) = 0. \tag{49}$$

Multiply Equation (43) by φ_{1s} and φ_{2s} ; for the two solar arrays, integrate the resulting equations across the domain $0 \leq x \leq L_1$, respectively; multiply Equation (44) by φ_{3s} ; integrate the resulting equations over the domain $0 \leq x \leq L_2$ for the deployable arm; multiply Equations (45)–(49) by X_{cs} , Y_{cs} , Θ_{cs} , Y_{rs} , and Θ_{rs} , respectively; apply the orthogonality relations in Equations (40) and (41); and add all of the resulting equations and Equations (8)–(10) of the boundary condition. We then have

$$M_s \ddot{q}_s + K_s q_s = \Theta_{cs} M_c, \quad s = 1, 2, \dots, n. \tag{50}$$

where K_s and M_s are the modal stiffness and modal mass of s-th, respectively.

3. Results and Discussion

In this section, the first eight mode shapes of the spacecraft with large flexible structures are provided. Then, the influence of the deployable antenna on the natural frequencies and global mode shapes of the flexible spacecraft is discussed and then compared with the influence as obtained from the finite element software ANSYS. Finally, the dynamic responses of the spacecraft under the attitude control torque are performed. Table 1 lists the physical parameters of the spacecraft.

Table 1. The parameters of the spacecraft.

Parameter	Value
Solar array length L_1 (m)	8
Solar array mass density ρ_1 (kg/m)	2.86
Solar array flexural rigidity $E_1 I_1$ (N · m ²)	4072
Deployable arm mass density ρ_2 (kg/m)	2.29
Deployable arm flexural rigidity $E_2 I_2$ (N · m ²)	9.78×10^5
Deployable arm length L_2 (m)	8
Distance $d_1 = d_2 = d_3$ (m)	1
Main-body mass m_c (kg)	640
Main-body moment of inertia J_c (kg · m ²)	426.7
Deployable antenna areal density (kg/m ²)	0.3
Deployable antenna diameter $2d$ (m)	20

For the finite element model, the solar arrays, the main-body, the deployable arm, and the deployable antenna are modeled by the BEAM 188 element, the SOLID 45 element, the PIPE 16 element, and the SOLID 45 element, respectively. The flexible spacecraft is divided into 12,892 elements. Table 2 shows that the first eight natural frequencies and global mode shape obtained from the proposed model were in excellent agreement with those obtained from ANSYS, such that the largest difference in natural frequencies was only 3.83%. In addition, the first eight mode shapes obtained by the proposed model were exactly the same as those from the model in ANSYS. All the above findings prove the validity of the dynamic model proposed here.

Table 2. The lowest eight natural frequencies of the bridge system ω (Hz).

	ω_1	ω_2	ω_3	ω_4	ω_5	ω_6	ω_7	ω_8
Proposed model	0.336	0.345	1.934	2.081	2.241	5.689	5.804	7.079
ANSYS	0.336	0.343	1.908	2.082	2.260	5.742	5.805	7.350

3.1. Mode Analysis

Figure 4 depicts the first eight global mode shapes of the flexible spacecraft. As illustrated in the figure, since the flexible spacecraft is a symmetrical T-shaped configuration, its global mode shapes show the characteristics of symmetry and antisymmetry. In the first mode shape, the translational displacement of the main-body in the vertical direction and the left and right solar arrays are the same. In the second mode shape, the main-body undergoes rotational displacement, the deployable antenna undergoes translational displacement in the horizontal direction and rotational displacement, and the left and right solar arrays are opposite. In the third mode shape, the main-body shows significant rotational displacement, the deployable antenna exhibits a small degree of horizontal and rotational displacement, and the left and right solar arrays are opposite. In the fourth mode shape, the translational displacement of the main-body in the vertical direction and the left and right solar arrays are the same. In the fifth mode shape, the main-body shows significant rotational displacement, the deployable antenna undergoes translational displacement in the horizontal direction and rotational displacement, and the left and

right solar arrays are opposite. In the sixth mode shape, the main-body shows significant rotational displacement, the deployable antenna exhibits a small degree of horizontal and rotational displacement, and the left and right solar arrays are opposite. In the seventh mode shape, the translational displacement of main-body in the vertical direction and the left and right solar arrays are the same. In the eighth mode shape, the main-body shows significant rotational displacement, the deployable antenna exhibits a small degree of horizontal and rotational displacement, and the left and right solar arrays are opposite.

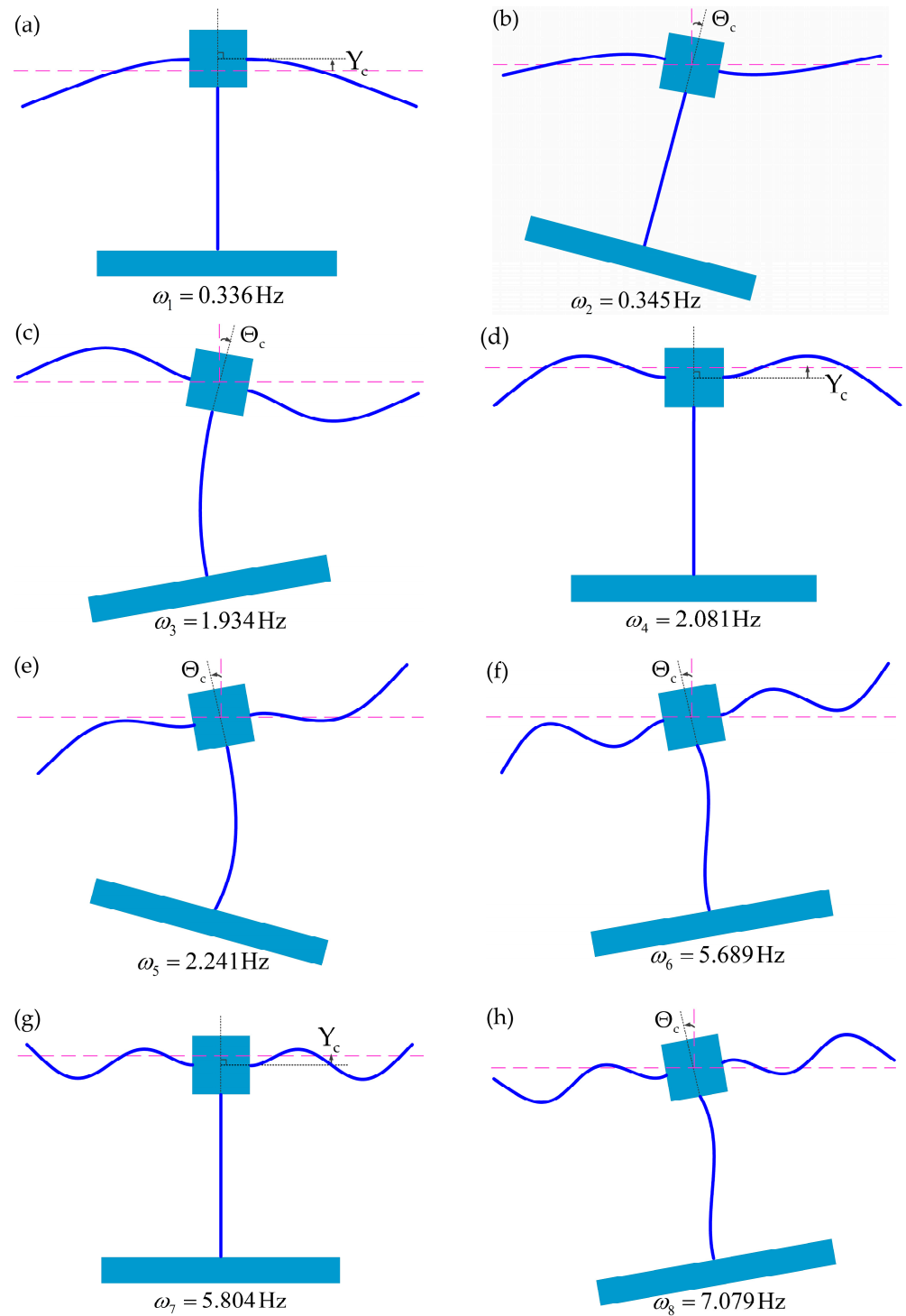


Figure 4. The flexible spacecraft’s first to eighth global mode shapes (a-h).

The first, fourth, and seventh mode shapes are symmetric, and the rest of the mode shapes are antisymmetric. The symmetrical mode shapes show the characteristic of local deformation, where only the solar wing is deformed. The antisymmetric mode shows global deformation, where the solar arrays and the deployable arm are both deformed.

In order to investigate the influence of the deployable antenna on the spacecraft, the natural frequencies of the spacecraft are calculated when the deployable antenna diameter varies from 5 to 30 m, as shown in Figure 5. It can be clearly seen that as the antenna diameter increases, the mode exchange phenomenon occurs with the frequency veering phenomenon. At antenna diameters of 28 m, 7 m, and 14 m, the interchange of first mode and second mode, the interchange of third mode and fourth mode, and the interchange of sixth mode and seventh mode occur, respectively. From Figures 4 and 5, it can be concluded that the mass and moment inertia of the antenna have a great influence on the natural frequency corresponding to the antisymmetric mode but almost no effect on the natural frequency corresponding to the symmetric mode. When the frequency veering phenomenon occurs, the symmetric and antisymmetric modes are interchanged with each other.

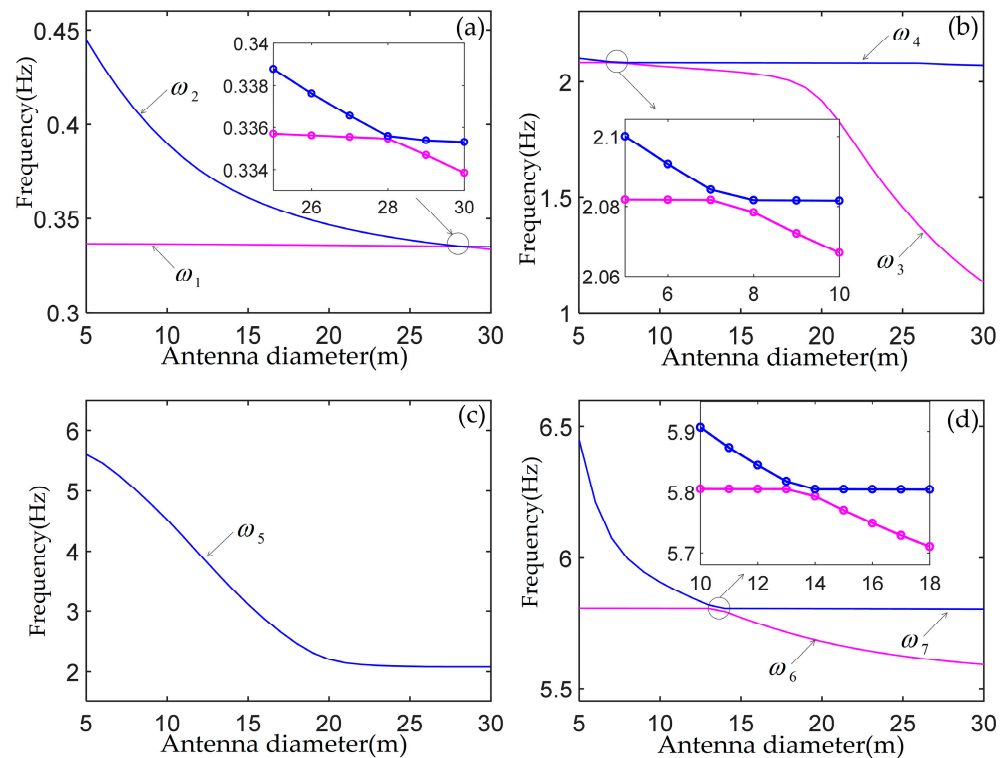


Figure 5. The first seven natural frequencies versus the deployable antenna diameter: (a) the first and second frequencies, (b) the third and fourth frequencies, (c) the fifth frequencies, (d) the sixth and seventh frequencies.

3.2. Dynamic Responses

The vibration response of the spacecraft with solar arrays and deployable antenna in the attitude maneuver is investigated in this section. It is assumed that the attitude control torque is

$$M_c(t) \begin{cases} M_0 \sin\left(\frac{2\pi}{T_M}t\right), & 0 \leq t \leq T_M, \\ 0, & t > T_M. \end{cases} \quad (51)$$

where T_M and M_0 are the period and amplitude of the attitude control torque, re-spectively. Figure 6 depicts the attitude control torque acting on the flexible spacecraft.

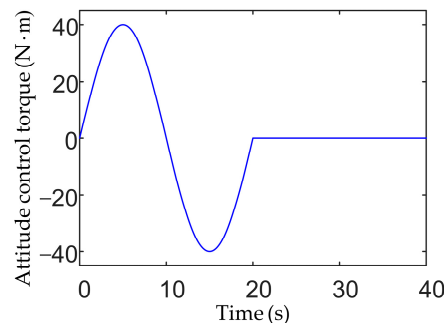


Figure 6. Time history of attitude control torque.

It is clear from Figure 4 that the symmetrical modes cannot be excited by attitude control torque. Therefore, there is no translational vibration response of the main-body in the vertical direction. In this case, the deployable antenna mass and moment of inertia are 94.25 kg and 2356 (kg·m²), respectively. The first 10 modes are selected to calculate the vibration responses of the flexible spacecraft, as shown in Figures 7–9.

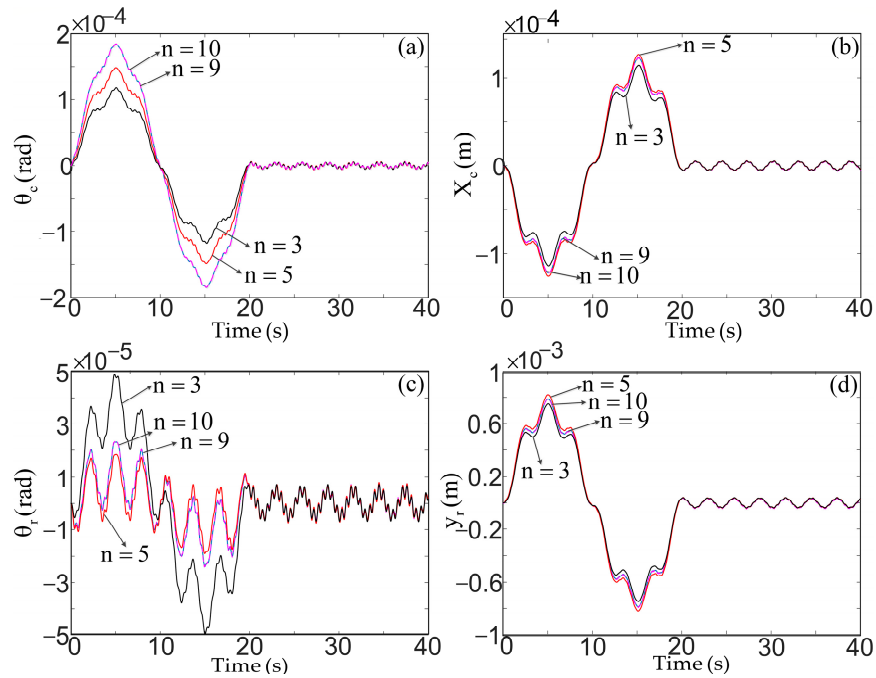


Figure 7. Vibration response of the main-body (a) rotation and (b) translation in horizontal direction, and the deployable antenna (c) rotation and (d) translation in horizontal direction.

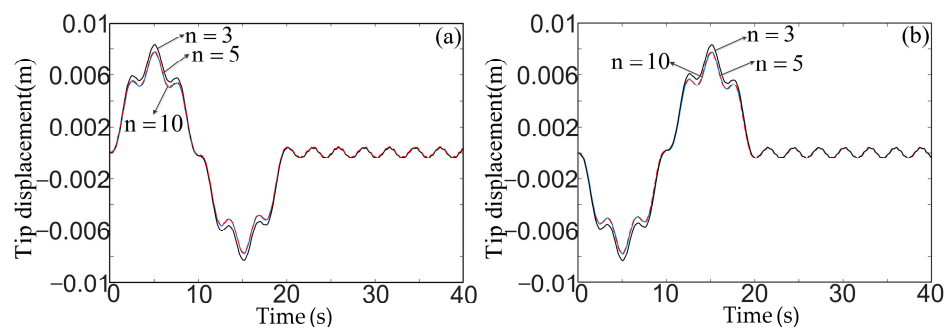


Figure 8. Vibration response of the solar array tip: (a) left and (b) right.

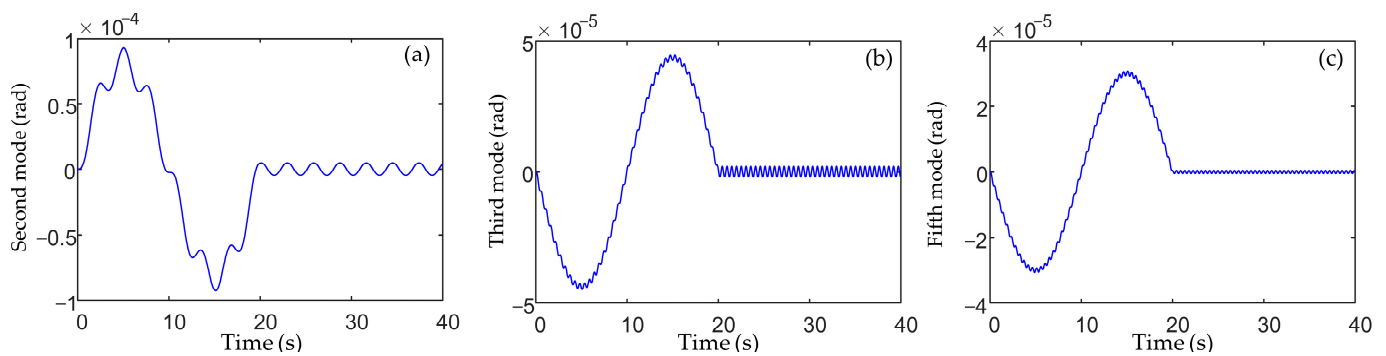


Figure 9. Vibration response of the deployable antenna: (a) second mode, (b) third mode, and (c) fifth mode.

Figure 7 demonstrates that the vibration amplitude of the main-body attitude is much larger than the vibration amplitude of the antenna attitude, and the vibration amplitude of the antenna in the horizontal direction is much greater than the vibration amplitude of the main-body in the horizontal direction. This indicates that the attitude control torque operating on the main-body has more influence on the horizontal translation of the antenna than on the attitude of the antenna. The rotational motion of the main-body and deployable antenna requires more degrees of freedom, and the number of degrees of freedom of its horizontal translation response has little impact on it. In addition, because the displacement of the second mode of the antenna cancels out the displacement of the third and fifth modes, as shown in Figure 9, the vibration response of the antenna appears different, as shown in Figure 7c. From Figure 8, since only the antisymmetric modes can be excited by the attitude control torque, the two solar arrays are deformed in the opposite direction.

4. Conclusions

A dynamic modeling approach has been described to obtain an analytical model for a spacecraft with large solar arrays and deployable antenna. The use of the natural frequencies, the global mode shapes, and their orthogonality relations results in fewer degrees of freedom for the decoupled analytical model of the flexible spacecraft, which is not only convenient for studying the system's nonlinear dynamic behavior, but also suitable for vibration control of the spacecraft with multiple large flexible structures.

The flexible spacecraft has been investigated taking into consideration various sizes of the deployable antenna, and the dynamic responses of the spacecraft have been calculated in the attitude maneuver. Some conclusions are summarized as follows:

- (1) Since the flexible spacecraft is symmetrical, its global mode shapes show the characteristics of symmetry and antisymmetry. As the diameter of the deployable antenna increases, the frequency veering phenomenon occurs, and the symmetric and the antisymmetric modes are interchanged with each other.
- (2) When the control torque is applied on the main-body to maneuver the attitude of the spacecraft, its influence on the horizontal position of the deployable antenna is much greater than the effect on the attitude of the deployable antenna.

Author Contributions: Conceptualization, J.W.; methodology, J.W.; software, W.L. and J.L.; investigation, writing—original draft, J.W., W.L. and J.L.; writing—review and editing, J.W., W.L. and T.Y.; visualization, W.L. and J.L.; supervision, J.W. and T.Y.; project administration, J.W. and T.Y. All authors have read and agreed to the published version of the manuscript.

Funding: This work was supported by the China Postdoctoral Science Foundation (Grant No. 2020M681578); the National Natural Science Foundation of China (Grant Nos. 12002298 and 11732005); and the Shandong Provincial Natural Science Foundation, China (Grant No. ZR2020QA038).

Data Availability Statement: Not applicable.

Acknowledgments: The authors gratefully acknowledge the support of the DQ research group, the Institute of Aerospace Vehicle Dynamics and Control, and the Harbin Institute of Technology.

Conflicts of Interest: The authors declare no conflict of interest.

References

1. Liu, Z.Q.; Qiu, H.; Li, X.; Yang, S.L. Review of large spacecraft deployable membrane antenna structures. *Chin. J. Mech. Eng.* **2017**, *30*, 1447–1459. [[CrossRef](#)]
2. Thomson, M. AstroMesh deployable reflectors for ku- and ka-band commercial satellites. In Proceedings of the 20th AIAA International Communication Satellite Systems Conference and Exhibit, Montreal, QC, Canada, 12–15 May 2002.
3. Imbriale, W.A.; Gao, S.S.; Boccia, L. *Space Antenna Handbook*; John Wiley & Sons: Hoboken, NJ, USA, 2012.
4. Thomson, M.W. The AstroMesh deployable reflector. In Proceedings of the IEEE Antennas and Propagation Society International Symposium, Orlando, FL, USA, 11–16 July 1999; Volume 1513, pp. 1516–1519.
5. Bohling, R.F.; Carroll, F.J.; Clark, J.P.; Debra, D.B.; Dobrotin, B.M.; Fischell, R.E.; Fleig, A.J.; Fosth, D.; Gatlin, J.A.; Perkel, H.; et al. *Spacecraft Radiation Torques*; National Aeronautics and Space Administration: Washington, DC, USA, 1969.
6. Palmerini, G.B.; Sgubini, S. Effects of the Solar Radiation Torque on Sun-Synchronous Gravity Gradient Stabilized Spacecraft. In Proceedings of the 54th International Astronautical Congress of the International Astronautical Federation, the International Academy of Astronautics, and the International Institute of Space Law, Bremen, Germany, 29 September–3 October 2003.
7. Li, W.; Xiang, Z.H.; Chen, L.J.; Xue, M.D. Thermal flutter analysis of large-scale space structures based on finite element method. *Int. J. Numer. Methods Eng.* **2007**, *69*, 887–907. [[CrossRef](#)]
8. Datashvili, L.; Tsignadze, N.; Santiago-Prowald, J. Study of mechanical architectures of large deployable space antenna apertures: From design to tests. *CEAS Space J.* **2013**, *5*, 169–184. [[CrossRef](#)]
9. Stegman, M.D.; Fedyk, M.; Kuehn, S. Solar Thermal Vacuum testing of deployable mesh reflector for model correlation. In Proceedings of the Aerospace Conference, Piscataway, NJ, USA, 31 October 2009.
10. Angeletti, F.; Gasbarri, P.; Sabatini, M. Optimal design and robust analysis of a net of active devices for micro-vibration control of an on-orbit large space antenna. *Acta Astronaut.* **2019**, *164*, 241–253. [[CrossRef](#)]
11. Mobrem, M. Methods of analyzing surface accuracy of large antenna structures due to manufacturing tolerances. In Proceedings of the 44th AIAA/ASME/ASCE/AHS Structures, Structural Dynamics, and Materials Conference, Norfolk, Virginia, 7–10 April 2003.
12. Ma, X.F.; Song, Y.P.; Li, Z.J.; Li, T.J.; Wang, Z.W.; Deng, H.Q. Mesh reflector antennas: Form-finding analysis review. In Proceedings of the 54th AIAA/ASME/ASCE/AHS/ASC Structures, Structural Dynamics, and Materials Conference, Boston, MA, USA, 8–11 April 2013.
13. Chodimella, S.P.; Moore, J.D.; Otto, J.; Fang, H.F. Design evaluation of a large aperture deployable antenna. In Proceedings of the 47th AIAA/ASME/ASCE/AHS/ASC Structures, Structural Dynamics, and Materials Conference, Newport, RI, USA, 1–4 May 2006.
14. Mobrem, M.; Kuehn, S.; Spier, C.; Slimko, E. Design and performance of Astromesh reflector onboard Soil Moisture Active Passive spacecraft. In Proceedings of the 2012 IEEE Aerospace Conference, Big Sky, MT, USA, 3–10 March 2012.
15. Angeletti, F.; Iannelli, P.; Gasbarri, P.; Gonzalez, J.A.P.; Ellero, N.; Wattrelot, T.; Ankersen, F.; Sabatini, M.; Celani, F.; Palmerini, G.B. Robust Collocated Control of Large Flexible Space Structures. *IFAC-PapersOnLine* **2022**, *55*, 85–90. [[CrossRef](#)]
16. Sabatini, M.; Gasbarri, P.; Palmerini, G.B.; Monti, R. Operational modal analysis via image based technique of very flexible space structures. *Acta Astronaut.* **2013**, *89*, 139–148. [[CrossRef](#)]
17. Ivanov, D.S.; Meus, S.V.; Ovchinnikov, A.V.; Ovchinnikov, M.Y.; Shestakov, S.A.; Yakimov, E.N. Methods for the vibration determination and parameter identification of spacecraft with flexible structures. *J. Comput. Syst. Sci.* **2017**, *56*, 311–327. [[CrossRef](#)]
18. Wang, Z.H.; Jia, Y.H.; Xu, S.J.; Tang, L. Active vibration suppression in flexible spacecraft with optical measurement. *Aerosp. Sci. Technol.* **2016**, *55*, 49–56. [[CrossRef](#)]
19. Liu, C.; Tian, Q.; Hu, H.Y. Dynamics of a large scale rigid–flexible multibody system composed of composite laminated plates. *Multibody Syst. Dyn.* **2011**, *26*, 283–305. [[CrossRef](#)]
20. Liu, L.K.; Shan, J.J.; Zhang, Y. Dynamics modeling and analysis of spacecraft with large deployable hoop-truss antenna. *J. Spacecr. Rocket.* **2016**, *53*, 471–479. [[CrossRef](#)]
21. Meirovitch, L.; Kwak, M.K. Dynamics and control of spacecraft with retargeting flexible antennas. *J. Guid. Control Dyn.* **1990**, *13*, 241–248. [[CrossRef](#)]
22. Salehian, A.; Seigler, T.M.; Inman, D.J. Control of the Continuum Model of a Large Flexible Space Structure. In Proceedings of the 2006 ASME International Mechanical Engineering Congress and Exposition, Chicago, IL, USA, 5–10 November 2006.
23. Neto, M.A.; Ambrósio, J.; Leal, R.P. Composite materials in flexible multibody systems. *Comput. Methods Appl. Mech. Eng.* **2006**, *195*, 6860–6873. [[CrossRef](#)]
24. Hablani, H.B. Dynamics and control of a deformable gyostat, utilizing continuum vehicle modes. *J. Guid. Control Dyn.* **1983**, *6*, 499–510. [[CrossRef](#)]
25. Hablani, H.B. Constrained and unconstrained modes: Some modeling aspects of flexible spacecraft. *J. Guid. Control Dyn.* **1982**, *5*, 164–173. [[CrossRef](#)]

26. Skelton, R.E.; Hughes, P.C.; Hablani, H.B. Order reduction for models of space structures using modal cost analysis. *J. Guid. Control Dyn.* **1982**, *5*, 351–357. [[CrossRef](#)]
27. Wei, J.; Cao, D.Q.; Huang, H. Nonlinear vibration phenomenon of maneuvering spacecraft with flexible jointed appendages. *Nonlinear Dyn.* **2018**, *94*, 2863–2877. [[CrossRef](#)]
28. Wei, J.; Cao, D.Q.; Wang, L.C.; Huang, H.; Huang, W.H. Dynamic modeling and simulation for flexible spacecraft with flexible jointed solar panels. *Int. J. Mech. Sci.* **2017**, *130*, 558–570. [[CrossRef](#)]
29. Wei, J.; Cao, D.Q.; Liu, L.; Huang, W.H. Global mode method for dynamic modeling of a flexible-link flexible-joint manipulator with tip mass. *Appl. Math. Model.* **2017**, *48*, 787–805. [[CrossRef](#)]
30. Wei, J.; Yu, T.; Jin, D.P.; Liu, M.; Cao, D.Q.; Wang, J.J. Nonlinear dynamic modeling and analysis of an L-shaped multi-beam jointed structure with tip mass. *Materials* **2021**, *14*, 7279. [[CrossRef](#)]
31. Wei, J.; Cao, D.Q.; Huang, H.; Wang, L.C.; Huang, W.H. Dynamics of a multi-beam structure connected with nonlinear joints: Modelling and simulation. *Arch. Appl. Mech.* **2018**, *88*, 1059–1074. [[CrossRef](#)]

Disclaimer/Publisher’s Note: The statements, opinions and data contained in all publications are solely those of the individual author(s) and contributor(s) and not of MDPI and/or the editor(s). MDPI and/or the editor(s) disclaim responsibility for any injury to people or property resulting from any ideas, methods, instructions or products referred to in the content.